Int. J. Electrochem. Sci., 15 **(2020)** 816 – 829, doi: 10.20964/2020.01.69

International Journal of
ELECTROCHEMICAL
SCIENCE
www.electrochemsci.org

Electrochemical corrosion resistance and wear behavior of Ni-P-ZrO_2 Composite Coatings prepared by Magnetically-Assisted Jet-Electrodeposition

Fu Xiu-qing[1,*], *Shen Mo-qi*[1], *Lin Jin-ran*[1],*Wang Xing-sheng*[1], *Wang Qing-qing*[1], *Xu Ye*[1]

College of Engineering, Nanjing Agricultural University, Nanjing 210031, P. R. China
[*]E-mail: fuxiuqing@njau.edu.cn

Received: 3 September 2019 / *Accepted:* 20 November 2019 / *Published:* 30 November 2019

Ni-P-ZrO_2 coatings were applied to #45 steel workpieces to extend their practical lifespans. With the assistance of a steady-state magnetic field, a Ni-P plating solution containing 50 nm ZrO_2 nanoparticles was used to electroplate a composite coating on the surface of #45 steel. The coating growth mechanism of both non-magnetically-assisted and magnetically-assisted coatings was established. Scanning electron microscopy (SEM), energy dispersive X-ray spectroscopy (EDS) and X-ray diffraction (XRD) were used to explore the microstructure and elemental composition of coatings. According to the analyses, the different properties of coatings, especially their corrosion resistance and wear resistance were significantly improved when a stable magnetic field was used. The use of a stable magnetic field during the coating application effectively improved its surface quality, nanoparticle content, hardness, corrosion resistance, and wear resistance.

Keywords: Steady magnetic field; Jet electrodeposition; ZrO_2 nanoparticles; Surface quality; Corrosion resistance; Wear resistance

1. INTRODUCTION

#45 steel is widely used in the production of gears, shafts, and various blank parts, but the failure of #45 steel parts often causes significant economic losses. To overcome this issue, electrochemistry, thermal spraying, electric spark, and laser techniques have been used to enhance the wear resistance of #45 steel [1-5]. Electrochemical methods provide an economical, fast, and efficient way to enhance the wear resistance by establishing coatings on the surface of steel. In recent years, jet electrodeposition coating has been shown to produce finer grains, a more uniform density, and better surface performance [6,7]. Some studies have even demonstrated a 2- to 3-fold increase in the hardness and wear resistance of surface coatings by using jet electrodeposition to add nanoparticles to coatings [8]. ZrO_2 nanoparticles are ceramic materials with excellent fire resistance, corrosion resistance, mechanical properties, and high ionic conductivities, and are often used in catalysts, fuel cells, gas sensors, and corrosion resistance materials [9-11]. Although jet electrodeposition has a high efficiency, the obtained coatings often have some defects, such as pits and bumps, which tend to be the origin of wear and tear. This paper solves these problems by adding an auxiliary magnetic field to traditional electroplating techniques to further improve and explore how a magnetic field influences the wear resistance of such coatings.

Magnetoelectrochemistry involves the application of a magnetic field during electrodeposition. Various literatures have studied how the application of a magnetic field changes the nucleation rate, hardness, grain growth, surface morphology, current efficiency, and other factors during electrodeposition [12-17]. Most studies have only combined electrodeposition with a magnetic field whose the direction coincides with the electric field. The Lorentz force only weakly affects the deposition mechanism of the coating. The bath flow rate of jet electrodeposition is higher, the direction is more dispersed, ions are subjected to magnetic disturbances, and the Lorentz force has a greater influence. In recent years, only one group [18] has obtained a relatively flat Ni-SiC alloy surface coating on the strongly magnetic material NdFeB by superimposing a magnetic field at the nozzle during jet electrodeposition.

In this paper, two growth mechanism models of non-magnetically-assisted (Ni-P-ZrO$_2$) and magnetically-assisted coatings (Ni-P-ZrO$_2$ (B)) are proposed. The coating sealing mechanism was verified by analyzing the surface microstructure and elemental composition of the coating. Finally, the effect of the new process on the wear resistance and corrosion resistance of the coating was verified and its mechanism was explored.

2. EXPERIMENTAL

2.1. General Experiment Outline

The diagram of the structure of the magnetically-assisted process is shown in Fig 1. A nozzle with a nickel rod was installed on the spindle of the machine tool to obtain a reciprocating movement. The nickel rod was connected to the anode of the DC power source for the oxidation reaction. The #45 steel workpiece was placed on a NdFeB magnetic platform which was connected to the cathode of the DC power source for the reduction reaction. During deposition, the plating solution was sprayed from the nozzle to the surface of the workpiece, forming a closed loop.

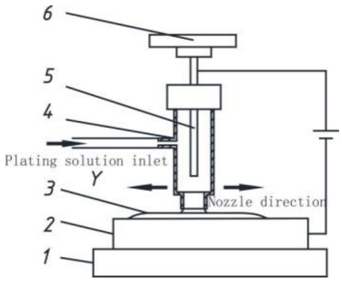

1. Magnetic platform; 2. Workpiece (45 steel); 3. Composite coating; 4. Nozzle; 5. Nickel rod; 6. Machine tool spindle.

Figure 1. Diagram of the structure of the magnetically-assisted jet electrodeposition platform.

The theoretical deposition model of traditional jet-electrodeposited Ni-P-ZrO_2 and Ni-P-ZrO_2(B) is shown in Fig 2. In Fig. 2 (a), under the action of an electric field, Ni^{2+} and H_3PO_3 gained electrons and formed Ni and P atoms, which were then deposited the workpiece surface. However, due to the tip effect, the electric field distribution was uneven, and many pits and bumps were formed on the surface of the coating and decreased its quality. However, it can be seen from Fig. 2(b) that the magnetic field improved the surface quality of the coating, which more evenly distributed the Ni^{2+} and H_3PO_3. According to the Gugliemi adsorption mechanism [20], ZrO_2 nanoparticles attracted and adhered to Ni^{2+} and then co-deposited on the substrate surface. As shown in Fig 2, under the influence of a magnetic field, the ZrO_2 nanoparticles maintained a certain distance from each other, increasing the relative adsorption area. At the same time, significantly fewer ZrO_2 nanoparticles agglomerated, enhancing the diffusion effect. Finally, Ni^{2+} on the surface of the ZrO_2 nanoparticles was reduced to Ni, and ZrO_2 nanoparticles became embedded in the coating to form a hard wear-resistant framework. At the same time, the Lorentz force acting on Ni^{2+} greatly increased the kinetic energy of the cations, accelerating the deposition reaction and increasing the surface deposition of Ni^{2+} [19].

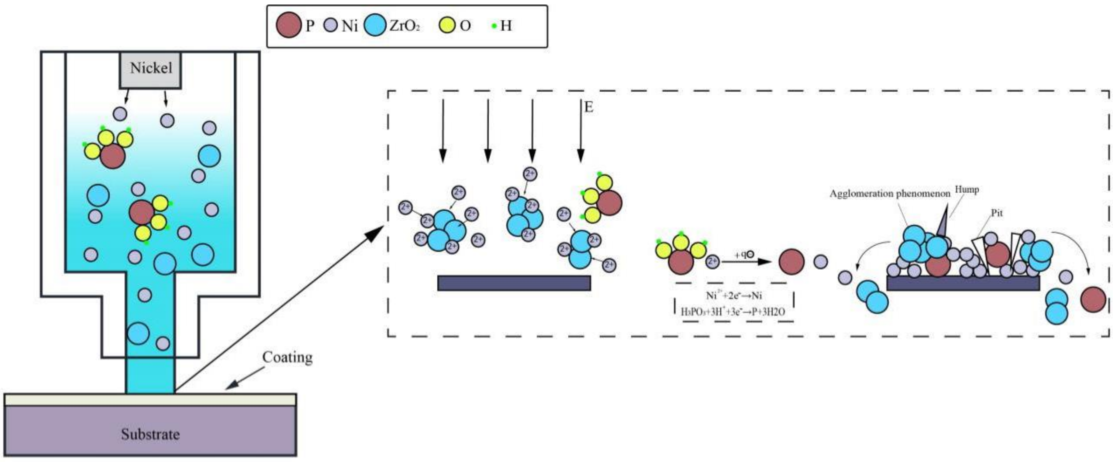

(a) Growth mechanism model of Ni-P-ZrO_2 coatings.

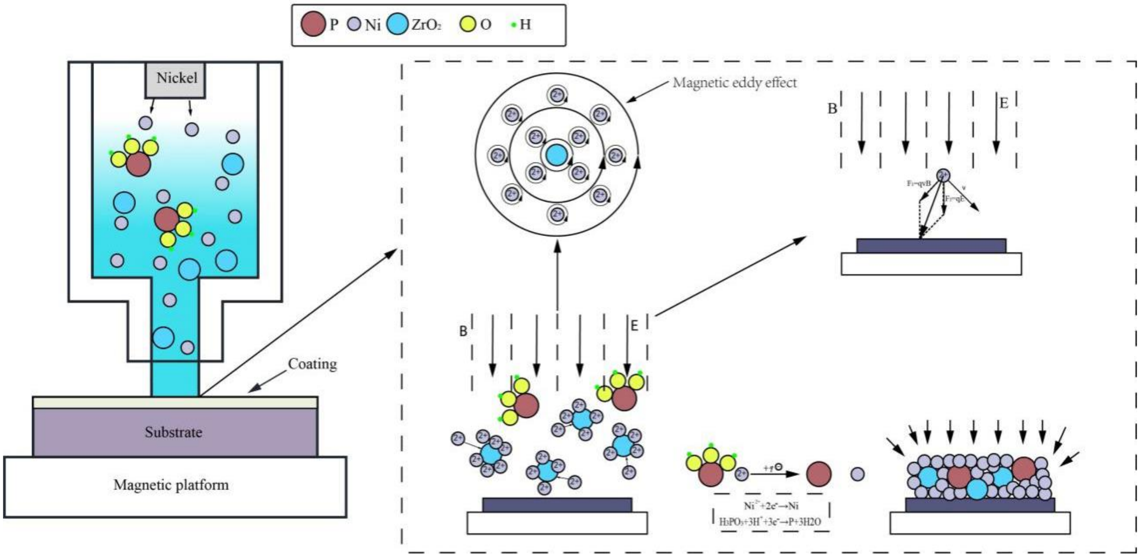

(b) Growth mechanism model of Ni-P-ZrO_2(B) coatings.

Figure 2. Comparison model of coatings growth mechanism.

2.2. Experimental

All chemicals were of analytical grade. Details of the plating solution and experimental conditions are shown in Table 1. #45 steel was used as the base metal with a sample size of 25 mm x 10 mm x 8 mm. The surface of the sample was polished successively by no. 40, no. 800, and no. 1500 wet-and-dry sandpaper until the metal surface was reflective ($R_a \leqslant 0.1$). The sample was then placed into alcohol and ultrasonically cleaned. Prior to jet electrodeposition, the workpiece was activated through the process steps shown below.

Oil removal → *ultrasonic cleaning* → *weak activation* → *ultrasonic cleaning* → *strong activation* → *ultrasonic cleaning*

A pure nickel rod was used as the cathode, and the #45 steel workpiece was used as the anode. The magnetic platform was made from NdFeB which provided a 0.3 T steady magnetic field. According to preliminary tests, it was found that a current intensity of 0.0024 A/mm^2 and a flow velocity of 4.5 m/s had the best effect on the processing area.

Table 1. Composition of the plating solution.

Ingredient	Content (g/L)
$NiSO_4 \cdot 6H_2O$	200
$NiCl_2 \cdot 6H_2O$	30
H_3PO_3	20
H_3BO_3	30
$C_6H_8O_7$(citric acid)	60
CH_4N_2S(thiocarbamide)	0.01
$C_{12}H_{25}SO_4Na$(lauryl sodium sulfate)	0.08
ZrO_2 nanoparticles (50 nm)	10

2.3 Instruments

A Quanta FEG 250 field emission scanning electron microscope (FE-SEM) from FEI Instruments, Inc. (USA) was used to investigate the surface morphology of samples using an accelerating voltage of 15 kV and a scan rate of 30 μs to obtain secondary electron images. Energy dispersive X-ray spectroscopy (EDS) (XFlash Detector 5030; Bruker AXS, Inc., Berlin, Germany) was coupled with the SEM and used to measure the ZrO_2 content. The accelerating voltage was 16 kV, the working distance was 11 mm, and scan area was 1 mm^2. A hardness measurement instrument (Duramin-40; Struers Inc., Denmark) was used for hardness determinations. The microhardness was measured by holding a 100 g load for 15 s, and reported values are the average of five replicates. The phase structure of the coating was analyzed using an X-ray diffractometer (PANalytical X'pert; PANalytical, Inc.) with a Cu Kα radiation source (λ = 0.15405 nm), operating voltage of 40 kV, scan rate of 5°/min, and scanning range (2θ) of 10°-80°. HighScore Plus software was used to analyze the XRD results. A CFT-I comprehensive property tester was used to mark the coating surface back and forth for 20 min, with a wear mark length of 4 mm and a load of 320 g. An Olympus LEXT 4100 laser confocal microscope (OLYMPUS, Japan) was used to measure the mark parameters. Electrochemical experiments were performed using a three-electrode cell on a CS350 electrochemical workstation (CS350, Wuhan Corrtest Instruments Corp., Ltd., China). During the test, the workpiece sample was encapsulated with epoxy resin, leaving an exposed area of 1 cm^2, and then immersed in a 50 g/L NaCl solution. Then, the potentiodymanic polarization curves of the coating was obtained by a potentiodynamic scanning method at a scan rate of 1mV s^{-1}, and then obtained by polarization curve epitaxy.

3. RESULTS AND DISCUSSION

3.1. Surface micromorphology, phase, and elemental content analysis

Fig. 3 and 4 respectively show the surface morphologies of Ni-P-ZrO_2(B) and Ni-P-ZrO_2(B) coatings as observed by SEM. Fig. 3(a) and 3(b) show that the coating surface had a cellular structure, but it contained obvious holes and bumps, indicating a poor surface quality.

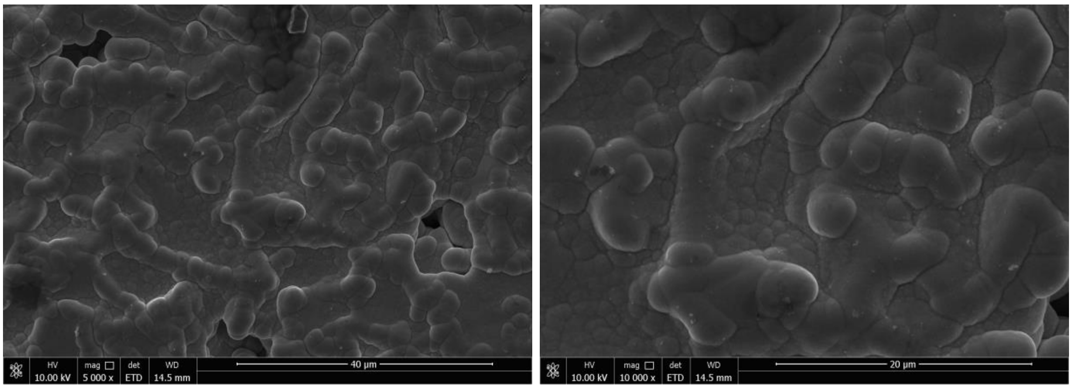

(a) (b)

Figure 3. Scanning electron micrograph of Ni-P-ZrO_2 coating (a) Magnification by 5000 times; (b) Magnification by 10000 times.

However, as shown in Fig. 4(a), 6(b), and 4(c), the Ni-P-ZrO_2(B) coating surface contained no obvious defects, and its cellular structure was flat and clear, indicating a high-quality coating. The X-ray diffraction patterns of the coatings in Fig. 5 show that a high-intensity diffraction peak appeared in the patterns of both coatings at 45°, which represents the (111) plane of face-centered cubic Ni. The peak was mostly sharp with some broadening, indicating that the coatings were composed of a mixture of amorphous and crystalline phases.

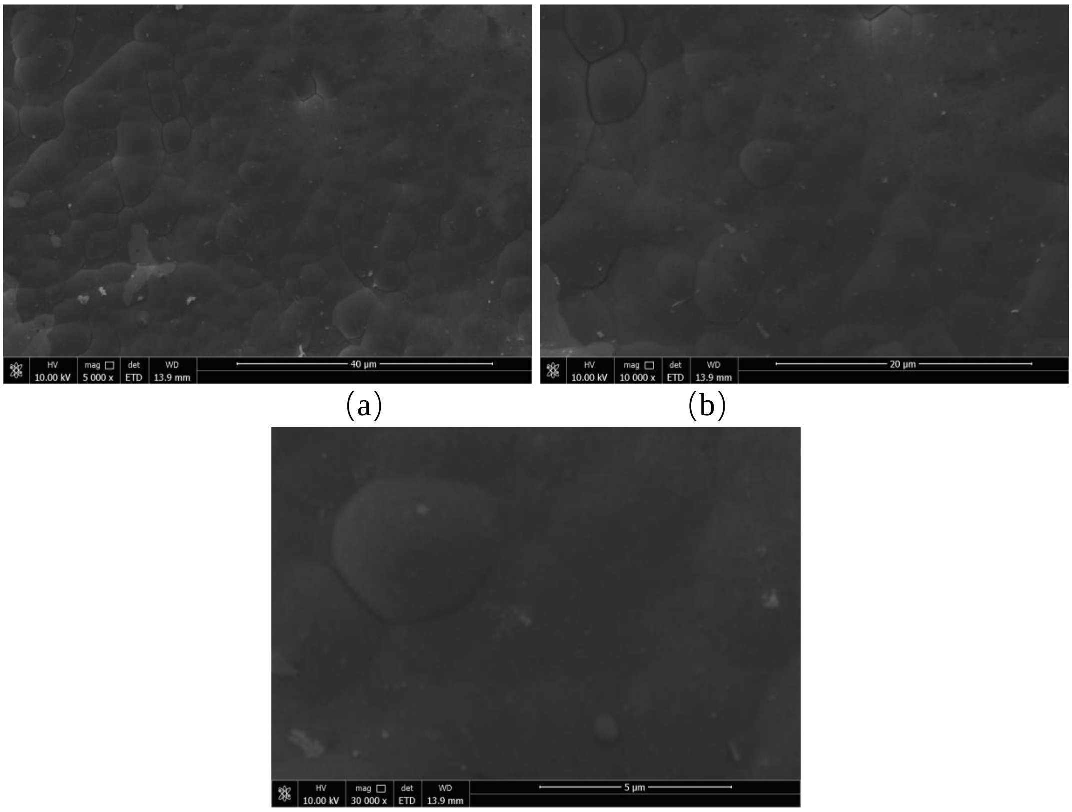

(a) (b)

(c)

Figure 4. Scanning electron micrograph of Ni-P-ZrO_2(B) coating (a) Magnification by 5000 times; (b) Magnification by 10000 times; (c) Magnification by 30000 times.

It can be seen from Fig. 6 that the Zr content in the Ni-P-ZrO_2(B) coating was higher than the coating obtained using traditional electrodeposition. The mass fraction of Zr increased from 4.15% to 4.61%, and the atomic fraction of Zr increased from 2.70% to 3.01%.

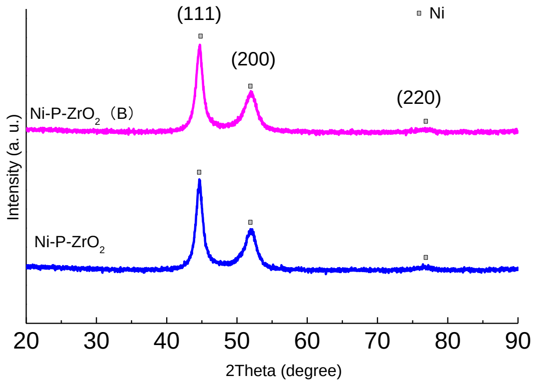

Figure 5. X-ray diffraction patterns of the coatings.

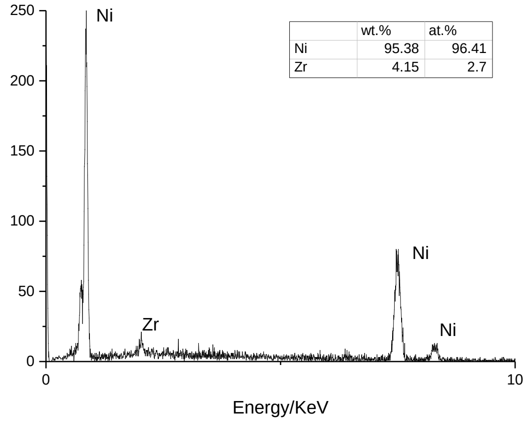

(a) Ni-P-ZrO_2 coating.

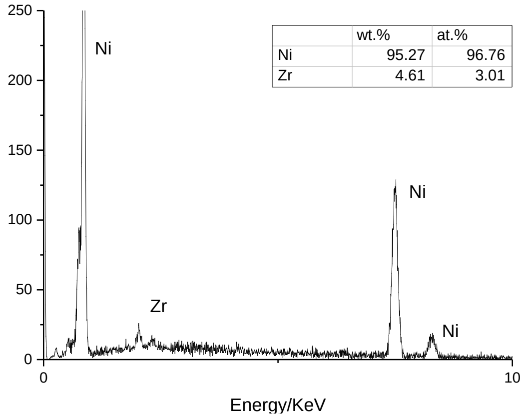

（b） Ni-P-ZrO_2(B) coating.

Figure 6. EDS spectra of coatings.

This indicates that Ni^{2+} was affected by both the electric field and the Lorentz force during deposition due to the magnetic field, which allowed more ZrO_2 nanoparticles and Ni^{2+} to be co-deposited on the workpiece surface. As a result, the Zr content in the coating increased, as shown in Fig. 6. As more ZrO_2 nanoparticles were introduced into the coating, its wear resistance increased. In the EDS spectra, Ni and Zr exhibited strong peaks, indicating successful electrodeposition (Fig. 6(a) and (b)).

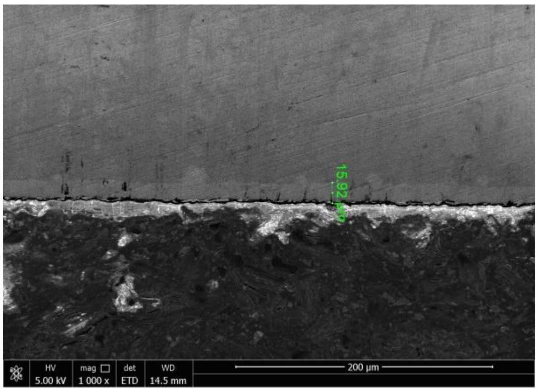

（a） Ni-P-ZrO_2 coating.

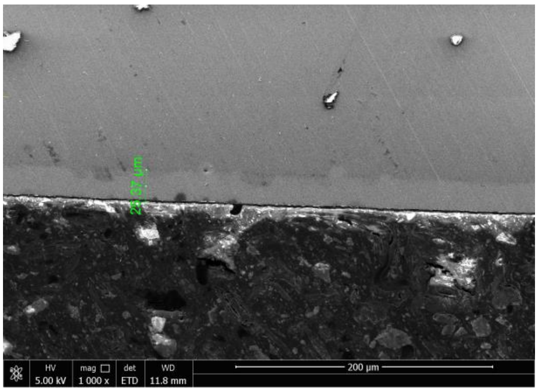

（b） Ni-P-ZrO_2(B) coating.

Figure 7. Cross-sectional SEM images of coatings.

The Zr content in the coating fabricated using traditional electrodeposition was 11.1% lower than in the coating obtained by magnetic platform assisted jet electrodeposition (4.61%). According to Fig. 6, more ZrO_2 nanoparticles were co-deposited when the magnetic platform was applied, which resulted in smaller cells and fewer grain boundaries.

The thickness of Ni-P-ZrO_2 coating in Fig. 7 was 15.92 µm, and that of the Ni-P-ZrO_2(B) coating was 25.37 µm. The coating growth rate V_g (µm/min) was calculated using the following formula:

$$V_g = \frac{H_g}{T}$$

where H_g represents the coating growth thickness (µm), and T represents the processing time (min). The growth rates were calculated to be 0.796 µm/min for Ni-P-ZrO_2 and 1.269 µm/min for Ni-P-ZrO_2(B). This indicates that electrons on the Ni^{2+} cathode surface were more efficient for deposition, and the coating grew faster due to the assistance of the magnetic field. The cross-section in Fig. 7 also shows the presence of many cracks in the Ni-P-ZrO_2 coating, while no cracks were observed in the cross-section of the Ni-P-ZrO_2(B) coating. The use of a magnetic field created a denser coating with fewer internal defects.

3.2 Hardness tests

The average hardness value (HV) of the Ni-P-ZrO_2 coating was 658.5 HV (Table 2), while the average hardness of the Ni-P-ZrO_2(B) coating was 12.3% higher at 739.3 HV. This occurred because there were many bumps and pits on the Ni-P-ZrO_2 coating surface, as shown in Fig. 3(a) and (b). In addition, the coating contained obvious cellular structure boundaries, which acted as damage points and reduced the hardness [21]. However, as shown in Fig. 4(a) and (b), no obvious defects were observed on the surface of the Ni-P-ZrO_2(B) coating. Its cellular structure was relatively flat and was not easily damaged when subjected to an external force, demonstrating an obvious improvement in the hardness of the coating. Previous studies have shown that the hardness of a coating directly affects its wear resistance, and materials with higher harness values tend to have a better wear resistance [22].

Table 2. Hardness measurement results.

Coatings	1 (HV)	2 (HV)	3 (HV)	4 (HV)	5 (HV)	Average (HV)
Ni-P-ZrO2	643.6	653.3	670.7	658.3	666.6	658.5
Ni-P-ZrO2(B)	735.5	753.0	736.5	725.8	745.7	739.3

3.3 Wear resistance

The measured friction coefficients of the two coatings are shown in Fig 8. As the friction test time increased, the friction coefficient of the Ni-P-ZrO_2 coating remained stable between 0.75 and 0.85, while that of the Ni-P-ZrO_2(B) coating was stable between 0.55 and 0.65. The friction coefficient of the Ni-P-ZrO_2 coating quickly reached equilibrium after an initial period, while the Ni-P-ZrO_2(B) coating went through a low friction coefficient phase (the dotted line in Fig 8), with a friction coefficient between 0.45 - 0.55 from 2.5 min - 12.5 min. This occurred because the oxide film present on the surface of the coating was protected by hard nanoparticles, which were not rapidly destroyed. Since the oxidation film has a self-lubricating effect, the friction coefficient at one stage in Fig. 8 was small [23], which improved the wear resistance of the coating surface. The wear resistance of the coatings was measured by observing the width and cross-sectional size of the wear mark by confocal microscopy, as shown in Fig. 9 and Table 3.

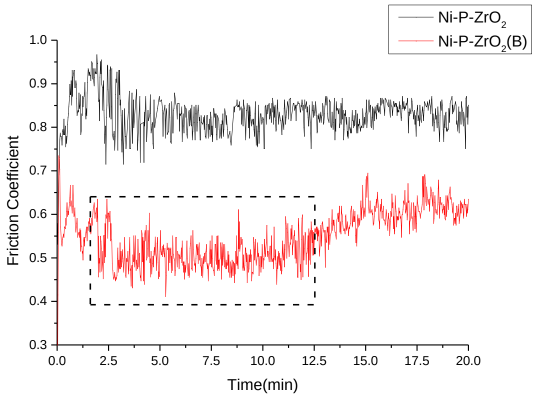

Figure 8. Friction coefficient measurements of the coating surfaces.

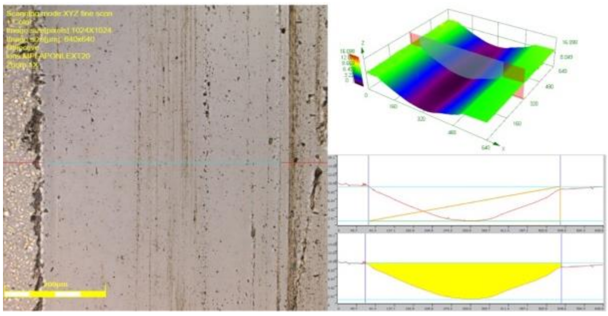

(a) Ni-P-ZrO_2 coating.

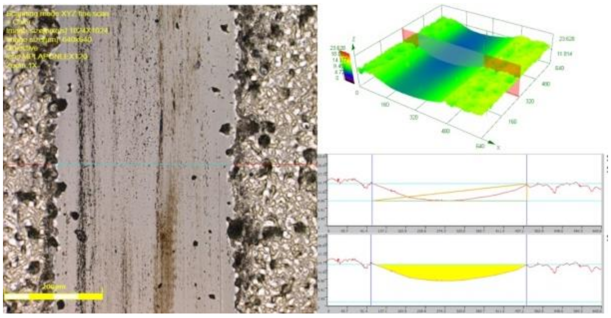

（b） Ni-P-ZrO_2(B) coating.

Figure 9. Scratch morphology of coatings.

Table 3. Scratch section parameters.

	Width (μm)	Height (μm)	Scratch area ($μm^2$)
Ni-P-ZrO_2	461.675	8.002	2498.395
Ni-P-ZrO_2 （B）	367.617	5.673	1288.155

The parameters listed in Fig. 9 and Table 3 show that the width, depth, and cross-sectional area of Ni-P-ZrO_2(B) coating were respectively 20.4%, 29.1%, and 48.4% smaller than those of the coating prepared without the assistance of a magnetic field. Thus, using a magnetic field greatly improved the wear resistance of the coating.

Fig. 9 shows the micromorphology of scratches on Ni-P-ZrO_2 and Ni-P-ZrO_2(B). Since the hardness of the GCr15 grinding balls was greater than the coating, the surface of the grinding ball was easily pressed into the coating. After pressing, the coating surface underwent plastic deformation, and atoms underwent cooperative binding which promoted adhesion. The plastic deformation zone easily hardened, which caused the coating to crack or even fall off [23,24]. From Fig 10(a) and 11(a), it can be seen that the Ni-P-ZrO_2 and Ni-P-ZrO_2(B) coatings contained some cracks around the wear marks because the partial crystalline and amorphous nature of the coating gave it excellent ductility. In addition, the amorphous phase showed good self-lubrication, which effectively prevented the coating from cracking [25]. From Fig. 10 (a), (b), and (c), it can be seen that there were a few wide furrows on the Ni-P-ZrO_2 surface, indicating that serious surface fatigue wear and abrasion had occurred on the coating, and one side of the coating fell off. The abrasive wear was caused by the uneven distribution of ZrO_2 nanoparticles on the surface of Ni-P-ZrO_2. After abrasion, agglomeration occurred locally, forming larger hard blocks. The agglomerated ZrO_2 nanoparticles had poor cohesion and were extruded from the surface during friction tests and formed several pits. The extruded aggregates had a higher hardness and easily adhered to the surface of the grinding ball, forming a hard "small blade" which further damaged the coating. This caused the coating to form larger pits, which seriously reduced the wear resistance of the coating itself. Fig 11(a), (b), and (c) show that the furrows of the Ni-P-ZrO_2(B) surface were close and narrow, which indicates that the coating surface had low fatigue and abrasive wear. This occurred because the embedded ZrO_2 nanoparticles formed a uniform wear-resistant framework in the presence of a magnetic field, effectively preventing the further expansion of furrows.

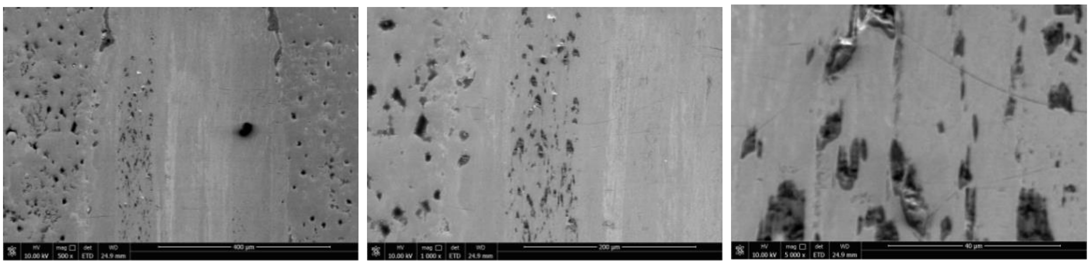
(a) (b) (c)

Figure 10. Scanning electron micrograph of the scratch on Ni-P-ZrO_2 coating. Magnification by 5000 times; (b) Magnification by 10000 times; (c) Magnification by 30000 times.

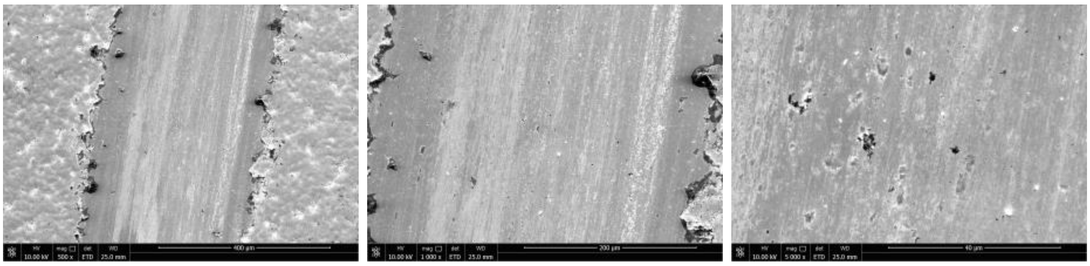
(a) (b) (c)

Figure 11. Scanning electron micrograph of the scratch on Ni-P-ZrO_2(B) coating. Magnification by 5000 times; (b) Magnification by 10000 times; (c) Magnification by 30000 times.

The Ni-P-ZrO_2 coating mainly suffered from surface fatigue and adhesive wear during wear tests, and due to the shedding of nanoparticles, severe local micro-cutting occurred. However, the Ni-P-ZrO_2 (B) coating had lower surface fatigue and abrasive wear due to the uniform dispersion of ZrO_2 nanoparticles. Thus, it can be concluded that the magnetic field assisted in the uniform dispersion of embedded ZrO_2 nanoparticles which formed a wear-resistant framework. This effectively improved the wear resistance of the coating and also reduced the degree of surface fatigue and abrasive wear.

3.4 Corrosion resistance

The corrosion resistance of coatings was tested using an electrochemical method with a three-electrode system. The work piece was a working electrode, a Pt sheet was used as the auxiliary electrode, and the reference electrode was a saturated calomel electrode (SCE). Potentiodymanic polarization curves and Nyquist plots were acquired at a scan rate of 1 mV $s^{-1}$from impedance measurements. Only 1 cm^2 of the work piece was immersed in a 3.5 wt% NaCl solution, and a potentiodynamic scanning method was used to record the potentiodymanic polarization curves of different coatings. Then, potentiodymanic polarization curves extension was used to determine parameters such as the corrosion potential and the corrosion current [26].

The potentiodymanic polarization curves of different coatings in 3.5 wt% NaCl solution (0.5 h) are shown in Figure 12. The corrosion potential E_{corr} and corrosion current density I_{corr}, obtained using the potentiodymanic polarization curves epitaxial method. According to Stern-Geary equation[26]:

$$i_{corr} = \frac{b_a \times b_c}{2.303 \times R_p(b_a + b_c)}$$

where b_a and b_c are the anodic and cathodic potentiodymanic polarization curves slopes, and R_p is the linear polarization resistance. With the assistance of Zview software, the corrosion potential E_{corr} and corrosion current density I_{corr} were calculated and shown in Table 5. The corrosion potential of Ni-P-ZrO_2 was -0.605 V, and the corrosion current density was 2.617 x 10^{-6} A·cm^{-2}, while the corresponding values of the Ni-P-ZrO_2 (B) composite coating were much higher at -0.465 V and 5.659 x 10^{-7} A·cm^{-2}, respectively. The corrosion potential increased by 24.66%, and the corrosion current density decreased by 78.37%.

The cross-sectional SEM images in Fig. 7 show that Ni-P-ZrO_2 (B) formed a more compact coating with tighter joints. When corrosion occurred, the corrosion resistance of the nickel-based coating depended on the surface density. After a steady-state magnetic field was applied, the number of surface defects significantly decreased, and the coating became denser, which increased the amount of time needed for the corrosive medium to infiltrate the substrate. Thus, the corrosion resistance increased, which decreased the electrochemical corrosion of the coating.

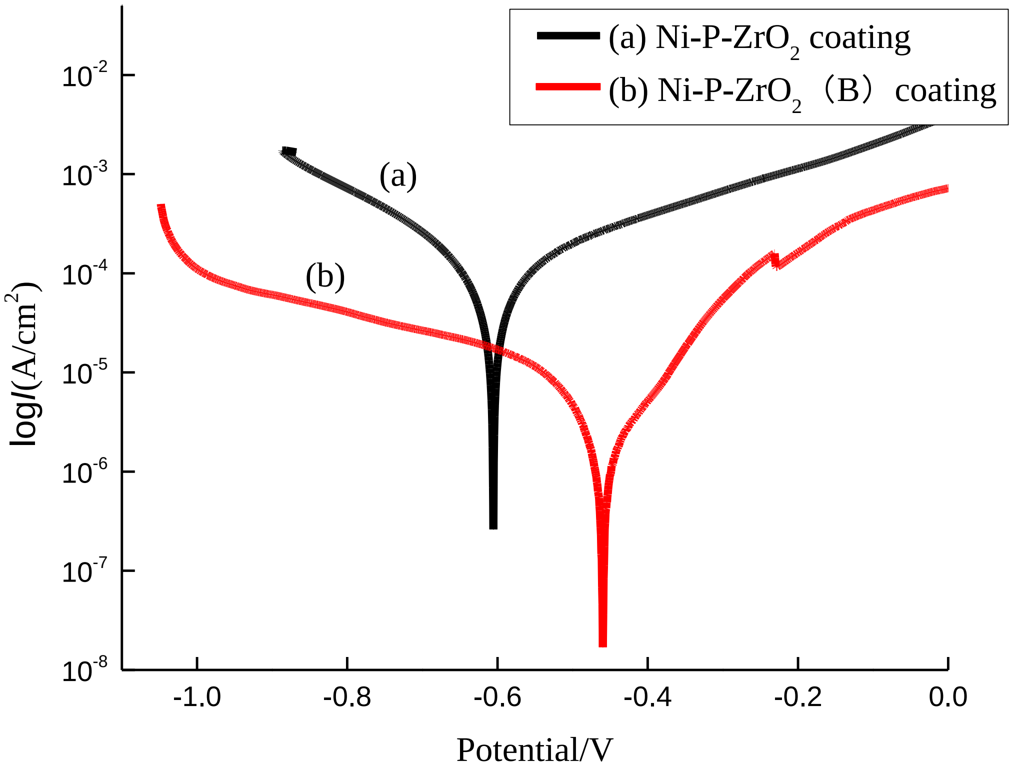

Figure 12. Potentiodymanic polarization curves of the coatings at a scan rate of 1 mV s^{-1}. (a) potentiodymanic polarization curves of Ni-P-ZrO_2; (b) potentiodymanic polarization curves of Ni-P-ZrO_2 (B)

Fig. 13(a) shows that corrosion occurred mainly at surface defects, and pitting corrosion occurred due to the presence of tiny gaps in the coating surface. Cl^- easily penetrated the substrate layer, which weakened the coating's protection [27]. Compared with Fig. 13(b), corrosion was more uniform due to the formation of a battery with ZrO_2 as the cathode and a metal coating as the anode. The formation of a corrosion cell effectively inhibited corrosion, making coatings more uniform and corrosion-resistant. In conclusion, the corrosion mechanism changed from point corrosion to uniform corrosion, which made the corrosion resistance polished.

Table 5. Corrosion potential (E_{corr}) and corrosion current density (I_{corr}) of samples.

Samples	E_{corr}/V	I_{corr}/A·cm^{-2}
Ni-P-ZrO_2	-0.605	2.617×10^{-6}
Ni-P-ZrO_2 (B)	-0.465	5.659×10^{-7}

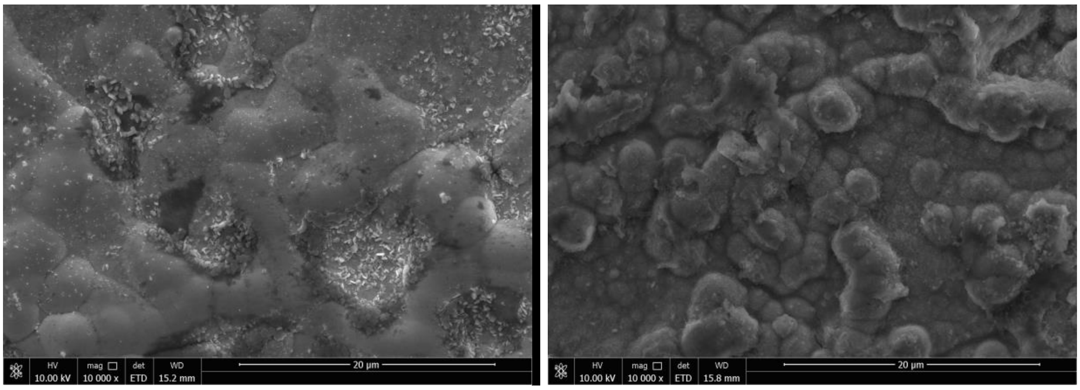

(a) **(b)**

Figure 13. Scanning electron micrographs of coatings after corrosion: (a) Ni-P-ZrO_2; (b) Ni-P-ZrO_2 (B).

4. CONCLUSIONS

(1) The Ni-P-ZrO_2 (B) coating prepared in the presence of a magnetic field showed a flatter surface and higher Zr content than a Ni-P-ZrO_2 coating prepared by traditional electrospray plating. The coating structure contained both amorphous and crystalline components.

(2) The surface hardness of the Ni-P-ZrO_2 (B) coating increased from 685.5 HV to 739.3 HV when a magnetic field was applied.

(3) Under the same friction test conditions, the Ni-P-ZrO_2 (B) coating showed better wear resistance than Ni-P-ZrO_2. Based on the microstructure, the Ni-P-ZrO_2 (B) coating mainly displayed only mild abrasive wear and surface fatigue wear, while the traditional Ni-P-ZrO_2 coating showed severe forms of both types of wear.

(4) Under the same corrosion conditions, the Ni-P-ZrO_2 (B) coating showed better corrosion-resistance than Ni-P-ZrO_2. The corrosion potential and the corrosion current density were significantly improved, and the corrosion mechanism changed from point corrosion to uniform corrosion.

ACKNOWLEDGEMENTS
Financial support for this work was provided by National Natural Science Foundationof China (Grant number 51705258), the China Postdoctoral Science Foundation (Grant number 2017M621665), the Postdoctoral Science Foundation of Jiangsu Province of China (Grant number 2018K022A).

References

1. Y. Zhao, W. He, H. Du and P. Luo, *Coatings*, 8 (2018) 297.
2. W. Ding, X. He, B. Xing and K. Zeng, *Hot Working Technol.*, 47 (2018) 1. (in Chinese)
3. Y. Zhang, W. Wang and J. Liao, *Trans. Chin. Soc. Agr. Eng.*, 33 (2017) 45. (in Chinese)
4. Y.J. Feng, D.M. Kan, X.D. Wei, N. Zhang, X.Y. Wang and H.B. Long, *Surf. Technol.*, 46 (2017) 75. (in Chinese)
5. H. Guo, X. Li and X. Cheng, *Welding Technol.*, 47 (2008) 1. (in Chinese)
6. B. Li, X. Li, Y. Huan, W. Xia and W. Zhang, *J. Alloys Compd.*, 762 (2018) 133.
7. M. Lekka, D. Koumoulis, N. Kouloumbi and P.L. Bonora, *Electrochim. Acta*, 54 (2009) 2540.
8. M. Kang, Y. Zhang and H.Z. Li, *Proc. CIRP*, 68 (2018) 221.
9. F. Heshmatpour and R.B. Aghakhanpour, *Powder Technol.*, 205 (2011) 193-200.
10. M. Tahmasebpour, A.A. Babaluo and M.K.R. Aghjeh, *J. Eur. Ceram. Soc.*, 28 (2008) 773.
11. T. Schmidt, M. Mennig and H. Schmidt, *J. Am. Ceram. Soc.*, 90 (2007) 1401.
12. R. Aogaki, K. Fueki and T. Mukaibo, *Denki Kagaku*, 43 (1975) 504.
13. T.Z. Fahidy, *J. Appl. Electrochem.*, 13 (1983) 553.
14. Q. Long, Y.Z. Zhang, F.H. Lu, Y.M. Luo, X. Luo and Y. Li, *Hydrometall. China*, 36 (2017) 288. (in Chinese)
15. C. Wang, Y.B. Zhong, J. Jia, Z.M. Ren, W.L. Ren and K. Deng, *Funct. Mater.*, 38 (2007) 3562. (in Chinese)
16. J.A. Koza, U. Mogi, K. Tschulik, M. Uhlemann, C. Mickel, A. Gebert and L. Schultz, *Electrochim. Acta*, 55 (2010) 6533.
17. M. Ebadi, W.J. Basirun, Y. Alias, M.R. Mahmoudian and S.Y. Leng, *Mater. Charact.*, 66 (2012) 46.
18. W. Jiang, L.D. Shen, M.B. Qiu, X. Wang, M.Z. Fan, and Z.J. Tian, *J. Alloys Compd.*, 762 (2018) 115.
19. F. Heshmatpour and R. B. Aghakhanpour, *Powder Technol.*, 205 (2011) 193.
20. N. Guglielmi, *J Electrochem Soc.*, 119 (1972) 1009.
21. H.Z. Li, M. Kang, Y. Zhang, X.F. Niu, C.H. Liu and M.F. Jin, *China Surf. Eng.*, 31 (2008) 103
22. B. Tang, P.Q. Wu, X.Y. Li, A.L. Fan, Z. Xu and J.P. Celis, *Surf. Coat. Technol.*, 179 (2004) 333.
23. C.X. Chen, Y.Q. Zuo, B.X. Liu and Y.Y. Li, *Surf. Technol.*, 47 (2018) 166. (in Chinese)
24. Q.C. Wang, N. Du, S.X. Wang and Q. Zhao, *Surf. Technol.*, 48 (2019) 191. (in Chinese)
25. C.Y. Luo, X.L. Ji and Z. Li, *China Surf. Eng.*, 30 (2017) 92. (in Chinese)
26. M.S. Beyragh, S.K. Asl and S. Norouzi, *Surf. Coat. Technol.*, 205 (2010) 2605.
27. T.P. Hoar, D.C. Mears, G.P. Rothwell, *Corros. Sci.*, 5 (1965) 279.